Hydrodynamics of liquid flow in a rotating cone

P.E. Dijk

Georgia Institute of Technology, School of Civil and Environmental Engineering, Altanta, Georgia, USA

A.M.C. Janse

DSM Food Specialities, DFS/R&D/R&F, Delft, The Netherlands

J.A.M. Kuipers and W.P.M. van Swaaij

Department of Chemical Engineering, Twente University, The Netherlands

Abstract *The average residence time of liquid flowing over the surface of a rotating cone was determined numerically. The development and propagation of the free surface flow was simulated using the volume of fluid (VOF) method. The numerical simulations were validated using laboratory experiments using soy-oil as a model liquid, and approximate analytical solutions of the simplified governing equations. The numerical simulations revealed the importance of the cone rotation frequencies and the minor influence of the cone angles on the residence times. Higher liquid throughputs produced smaller residence times. As expected, an increasing cone size results in proportionally higher residence times. Furthermore, it was established that even for small cones with a characteristic diameter of, e.g. less than 1m, relatively high (~1 kg/s) throughputs of liquid are possible. It appears that the combination of the decreasing layer thickness and the increasing size of the numerical grid cells with increasing radial cone coordinate hampers the numerical simulation of this system.*

Nomenclature

Roman

c	= constant
d	= distance, layer thickness m
d_o	= outer cone diameter m
f	= function
F	= fraction of volume
Fr	= Froude number defined by equation (16c)
g	= gravitational acceleration m/s^2
i,j	= cell indices in r-, θ-direction
M	= mass flow kg/s
n	= rotation frequency 1/s
$\mathbf{n}$	= normal vector
p	= static pressure Pa
P	= dimensionless static pressure
Q_0	= volumetric flow rate m^3/s
Q_0^+	= dimensionless volumetric flow rate
r	= radial spherical coordinate
r_o	= outer cone radius m
s	= distance from cone wall m
t	= time coordinate s

U	= dimensionless r velocity component
v	= velocity m/s
V	= volume m^3
V	= dimensionless θ velocity component
W	= dimensionless ϕ velocity component

Greek

δ	= Dirac function
δ^+	= dimensionless film thickness
θ	= angular spherical coordinate rad
ϕ	= rotational spherical coordinate rad
η	= dimensionless r-coordinate
λ	= dynamic bulk viscosity Pa s
μ	= dynamic shear viscosity Pa s
ν	= kinematic viscosity m^2/s
ρ	= density kg/m^3
σ	= dimensionless distance from cone wall
τ	= stress Pa
θ	= angular spherical coordinate
Θ	= dimensionless constant
ω	= angular frequency Hz
Ω	= angular frequency rad/s

Sub- and superscripts		o	= outflow, outlet
a	= atmospheric	s	= surface
i	= inflow, inlet	w	= wall, half top angle of cone

1. Introduction

Rotating cones have important applications as, e.g. liquid atomizers in oil burners (Hinze and Milborn, 1950) and liquid film evaporators (Bruin, 1969). Recently, they have also been used as reactors for rapid thermal processing of solids, e.g. for the flash pyrolysis of biomass (Wagenaar *et al.*, 1994a, 1994b) or polymer (Westerhout, 1998a, 1998b) particles. In this case, sand mixed with reactive particles, serves as a heat carrier and is used to prevent fouling of the cone wall. The main advantages of such systems are short residence times, high heating rates of the reactive particles and the absence of carrier gas since the rotation of the cone drives the particle transport.

In the latest design (Janse *et al.*, 1999), internal recirculation of sand is realized by partly submerging a cone with through-flow openings at its base into a fluidized bed of particles (i.e. sand and reactive particles). The particles flow via these openings into the cone and move upward along the inner cone wall along spiral trajectories. In the meantime, the reactive particles are converted to mainly gaseous products. When the sand passes the upper edge of the cone wall, it falls back into the fluidized bed. This reactor design allows for potentially thick, dense layers of particles to flow at high flow rates. A schematic representation of the prevailing gas-solids flow inside the rotating cone reactor is shown in Figure 1.

For a reliable design of such rotating cone reactors, the residence times and mass flow rates of the particles need to be known. The residence times determine the maximum allowable particle size of the feed and therefore influence the grinding costs. However, they are a complex function of the cone dimensions and rotation frequency, and the mass flow rate.
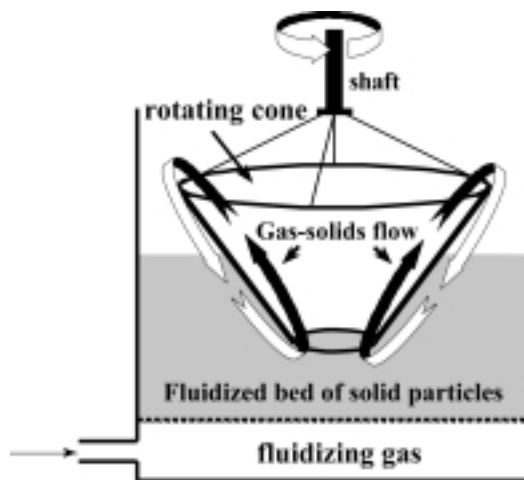

Figure 1.
Internal recirculation of
sand in the rotating
cone reactor

The only existing laboratory experiments were performed in two pilot plants of a rotating cone reactor with fixed dimensions (Wagenaar *et al.*, 1994a, 1994b; Janse, 1998). A thorough investigation based on laboratory experiments is not feasible, due to the expenses involved in creating and operating large numbers of rotating cones for the full range of parameter variation. In addition, it is very difficult to measure the layer thickness accurately, due to the combination of small layer thicknesses, small particle densities in the upper boundary layer and the bouncing nature of the particle movement. Consequently, theoretical models and numerical simulations of particle transport along rotating cone walls are necessary.

The only existing numerical simulation of particle transport in rotating cones was developed for a small number of bouncing particles (Wagenaar *et al.*, 1994b). Recently, discrete particle tracking simulations in Cartesian coordinates have been developed that take into account interactions between large numbers of particles and particle size distributions (e.g. Hoomans *et al.*, 1996, 2000). However, due to computational expenses these simulations cannot adequately describe the observed thick, dense layers containing ~106 to ~108 particles.

In a more practical approach, the gas and solid particle mixture can be described as two separate, fully interpenetrating continuum phases (e.g. Kuipers *et al.*, 1992). However, such a description is expected to be highly complex because of the free surface boundary conditions and spherical coordinates. Alternatively, as a first approximation, it can be assumed that the thick, dense granular flow is similar to the flow of a viscous, non-Newtonian fluid. The advantage of this one-fluid approach compared to the two-fluid approach is that it is conceptually simpler and easier to solve.

Ideally, analytical solutions of the governing equations of mass and momentum that describe the system are preferred. However, the development of analytical solutions for non-Newtonian fluid flows with free surface boundaries, partial slip condition at the cone wall and complex inflow and outflow conditions in spherical coordinates, as can be expected for sand flow in a rotating cone, is not realistic due to the complexity of the system. Existing approximate analytical solutions for fluid flow in rotating cones (Bruin, 1969) are based on highly simplified Navier-Stokes equations. They are only valid for Newtonian fluids with a no-slip flow condition at the cone walls, and only for special cases (e.g. very low, intermediate and very high rotation frequencies). Therefore, these analytical solutions cannot be used as a starting point for the description of sand flow, which is the ultimate goal of this study. In contrast, numerical simulations do not have these disadvantages, since their extension to other rheologies and boundary conditions is straightforward. However, to the best of our knowledge, numerical simulations of fluid flow in a rotating cone with free surface boundaries in spherical coordinates do not exist. Therefore, a method is developed to describe Newtonian fluid flow using finite difference techniques in combination with free surface tracking methods in spherical coordinates. The numerical simulations will be validated by laboratory observations using a number of different rotating cones and analytical solution for Newtonian fluid flow. After validation, the method will be extended to

non-Newtonian fluids and partial slip condition at the cone walls, and validated using laboratory observations of sand flow in rotating cones. These numerical simulations will then serve as the basis of much more comprehensive numerical simulations of two-phase sand-gas flow.

2. Methodology

Within the framework of the one-fluid approach, the granular flow prevailing in a rotating cone is governed on a microscopic scale by a set of mass and momentum conservation equations. These equations are derived from the general conservation equation applied to mass and momentum transport and simplified by making suitable approximations. We compute the transient solution of these equations, while only the final, steady state solution will be compared to the experimental observations and the analytical solutions. The conservation equations are supplemented with initial and boundary conditions. An additional complication that arises here is the fact that the free-surface location and associated boundary condition enforcement has to be dealt with.

2.1 Model assumptions

First, assumptions are made to simplify the governing mass and momentum conservation equations. It should be noted that the flow domain is restricted to the region inside the rotating cone. To describe this system, spherical coordinates in three dimensions (r, θ and ϕ) are appropriate where in addition the time coordinate (t) is required to study transient effects. The origin of the spherical coordinate system is situated at the virtual tip of the cone. Therefore, the spherical coordinates have the ranges $r_i \leq r \leq r_o$, $0 \leq \theta \leq \theta_w$ and $0 \leq \phi \leq 2\pi$ as indicated in Figure 2. In this study it will be assumed that the gas-solids flow in the rotating cone is symmetrical in the direction of rotation and therefore all quantities describing the flow are independent of ϕ

$$\frac{\partial}{\partial \phi}(..) = 0. \tag{1}$$

It is assumed that the mixture density (i.e. porosity) is constant and that the mixture layer is at least several solid particles thick. If in addition a tight
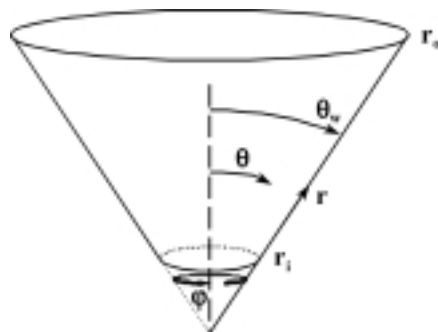

Figure 2.
Applied spherical
coordinate system

momentum coupling between the gas and solids phase exists, the gas-solids mixture can be treated as a single fluid, with a constant density ρ related to the constant porosity ε, and the constant density of the solids ρ_s and the gas ρ_g

$$\rho = \rho_s(1 - \varepsilon) + \rho_g \varepsilon. \tag{2}$$

The bulk gas is treated as a void, having no properties except that it takes up the space left by the fluid and that it possesses an atmospheric pressure. The characteristic quantities of the single fluid are the r-, θ- and ϕ- components of the velocity vector and the internal pressure. The location of the free surface between the fluid and the void is marked and traced according to the volume of fluid (VOF) method, as will be explained in section 2.2. In terms of the internal viscous stresses, the single fluid is assumed to behave like a Newtonian fluid. Finally, the gravitational force acting on the mixture of gas and solids is expressed by the components of the governing gravitational constant

$$\mathbf{g} = (-g \cos \theta, g \sin \theta, 0) \tag{3}$$

2.2 Model equations
When the assumptions mentioned above are applied to the mass and momentum conservation equations, their simplified versions specific to a single fluid flow in a rotating cone are obtained. They are presented below in vector form (Bird *et al.*, 1960) for the conservation of mass

$$\rho(\nabla \cdot v) = 0 \tag{4}$$

and the conservation of momentum

$$\rho \frac{\partial(v)}{\partial t} + \rho[\nabla \cdot vv] + \nabla p + [\nabla \cdot \tau] - \rho \mathbf{g} = 0 \tag{5}$$

where v is the flow velocity, p the pressure and τ the stress tensor. As mentioned before, the single fluid is assumed to behave like a Newtonian fluid. Therefore, the stress tensor is given by

$$\tau = -\mu\{\nabla v + \nabla v^T\} + \left(\frac{2}{3}\mu - \lambda\right)(\nabla \cdot v)\delta, \tag{6}$$

where μ and λ are the dynamic and shear fluid viscosities, respectively.

The application of a single fluid approach makes it necessary to define and trace the Eulerian location of the free surface. In our study the VOF method (Nichols *et al.*, 1980; Hirt and Nichols, 1981) was applied to deal with this complicated problem. Within the framework of the VOF method the fractional amount of fluid F is invoked to track the interface in the computational domain. The fractional amount of fluid distinguishes the fluid from the void and is defined as $F = 1$ if only fluid is present at the location (r, θ) and $F = 0$ if only void is present at location (r, θ). The free surface is defined by the discontinuity

in the fraction of volume, as shown in Figure 3. The development of the free surface is propagated as a Lagrangian invariant described by the partial differential free surface equation

$$\frac{\mathrm{D}F}{\mathrm{D}t} = \frac{\partial F}{\partial t} + (\nabla \cdot Fv) = 0. \tag{7}$$

The implementation and application of the VOF method in spherical coordinates is described in Janse *et al.* (2000) in detail.

2.3 Initial and boundary conditions
The initial conditions for $t = 0$ are described by zero values for the r-, θ-, and ϕ-velocity components, and the pressure $v_r = v_\theta = v_\phi = p = 0$ (i.e. fluid at rest). The initial fraction of volume F is prescribed, with unity for the space occupied by the fluid and zero for the space occupied by the void $F = \{0,1\}$. The cone inlet at $r = r_\mathrm{i}$ is described by a prescribed mass flow rate

$$\dot{M}(r_\mathrm{i}) = 2\pi r_\mathrm{i}^2 \int\limits_{\theta=0}^{\theta_\mathrm{w}} v_{r_\mathrm{i}}(\theta) \sin\theta\mathrm{d}\theta \tag{8}$$

from which r-direction inflow velocity component v_{r_i} is extracted. A tangential free-slip condition for the θ- and ϕ- velocity components $\partial v_\theta/\partial r = \partial v_\phi/\partial r = 0$, and a zero-gradient condition for both the pressure and the fraction of volume $\partial p/\partial r = \partial F/\partial r = 0$ are used. The continuative outlet at $r = r_\mathrm{o}$ implies a zero-gradient condition for the r-velocity component $\partial v_r/\partial r$, a tangential free-slip condition for the θ- and ϕ-velocity components $= \partial v_\theta/\partial r = \partial v_\phi/\partial r = 0$, and a zero-gradient condition for the pressure $\partial p/\partial_r = 0$. The prescribed fraction of volume is $F = 0$ for a non-outflowing system and $F = 1$ for an outflowing system. The fully continuative central symmetry line at $\theta = 0$ is described by a zero-gradient condition for the r-, θ- and ϕ-velocity components, the pressure, and the fraction of volume $\partial v_r/\partial\theta = \partial v_\theta/\partial\theta = \partial v_\phi/\partial\theta = \partial p/\partial\theta = \partial F/\partial\theta = 0$. The impermeable no-slip rotating cone wall is described by zero values for the r- and θ-velocity components $v_r = v_\theta = 0$, ϕ-velocity components equal to the velocities of the rotating wall

$$v_\phi = \Omega r \sin\theta_\mathrm{w}, \tag{9}$$

and a zero-gradient condition for the pressure and the fraction of volume $\partial p/\partial\theta = \partial F/\partial\theta = 0$. The coordinates of the free-surface boundary are expressed
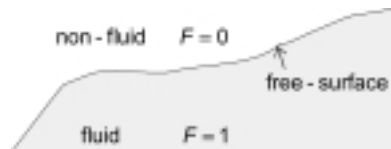

non - fluid   F = 0

free - surface

fluid   F = 1

by either their r-coordinates as a function of θ as $R(\theta)$, or by its θ-coordinate as a function of r as $\Theta(r)$. The boundary conditions for the free surface are described by a zero-gradient in normal direction for the tangential velocity $\theta v_t/\partial \mathbf{n} = 0$ and a prescribed atmospheric pressure $p = p_a$. The pressure condition incorporates the inviscid fluid conditions for the normal stress.

2.4 Numerical simulations

The conservation equations for mass and momentum (equations 4 and 5) are discretized according to the semi-implicit finite difference approximation for staggered fixed Eulerian grid cells. An example of such a grid is depicted in Figure 4. Subsequently, the fluid flow variables are computed iteratively via a pressure correction technique employing a whole field solution strategy (Kuipers *et al.*, 1992; Hirt and Nichols, 1981).

Due to the explicit treatment of momentum convection and viscous interaction terms, the time interval Δt must meet the Courant convective stability condition and the viscous stability condition. The convective stability condition states that the fluid is not allowed to move through more than one grid cell per time interval Δt

$$\Delta t < \min_{\substack{i \in [1,\ i_{max}] \\ j \in [1, j_{max}]}} \left(\frac{\Delta r}{|v_{r,i,j}|}, \frac{\Delta \theta}{|v_{\theta,i,j}|} \right) \tag{10}$$

whereas the viscosity stability condition states that the viscous momentum is not allowed to be transported through more than one grid cell per time interval Δt

$$\Delta t < \min_{i \in [1, i_{max}]} \left(\frac{1}{2} \frac{\Delta r^2 (r_i \Delta \theta)^2}{\Delta r^2 + (r_i \Delta \theta)^2} \frac{\rho}{\mu} \right) \tag{11}$$

to ensure numerical stability. Both conditions should be fulfilled over the entire computational domain occupied by the fluid. At the singular point $r_i = 0$, the point
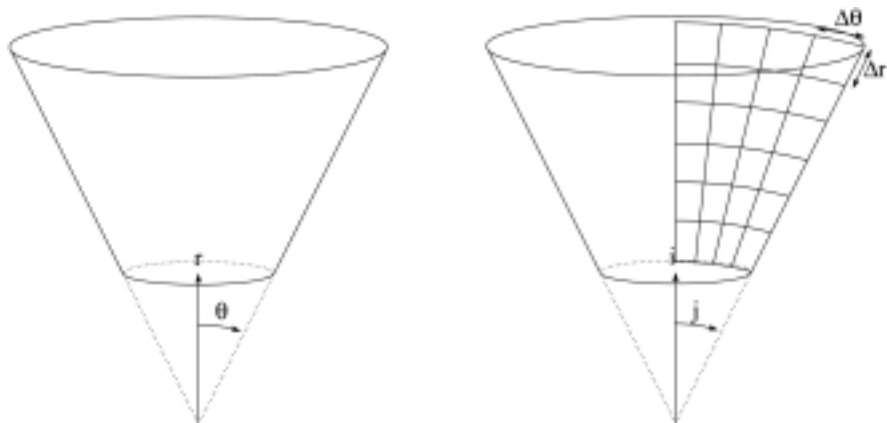

Figure 4.
Continuous (left) and discrete (right) coordinates

$r_i = \Delta r$ is used in the above expression and a safety margin is taken to ensure stability for this particular point. The singular symmetry line $\theta = 0$ (the central axis of the cone) is treated with special care. This singular point affects the convection and the diffusion term of the θ-component and the diffusion term of the θ-component of the momentum conservation equation. The relevant parts of these terms are set to zero for $\sin\theta = 0$.

At the cone inlet relatively thick layers develop, suggesting a coarse grid in the θ-direction. However, at the cone outlet, relatively thin layers are encountered, requiring a fine grid. Therefore, a variable grid size approach is used to improve the calculation efficiency. Typically, a grid size of 100 cells in the r-direction and six cells in the θ-direction is applied. The reason for the small number of grid cells in the θ-direction will be explained later. The calculations are performed on a personal computer with an Intel Pentium Pro 200-MHz processor. Typical computation times are in the order of six to ten hours.

2.5 Experimental set up

To validate the numerical simulations, experiments were conducted in which the thickness of a flowing liquid layer was measured as a function of the radial coordinate along the cone wall for several cone geometries. Since the cone angle and the inlet diameter D_i are the two most important cone parameters, they were varied systematically. Four different wall angles θ_w and two different inlet diameters D_i and cone heights H were applied, yielding a total of eight cones. For practical purposes, only the range of approximately $20 < \theta_w < 50°$ is interesting. The dimensions of the rotating cone are fixed by specifying one more cone dimension, for instance the outlet diameter D_o or equivalently the cone height H. To measure the thickness of the liquid layer, it is desirable to use a cone with an easily accessible top and inside. Therefore, the cone is open at the top and the motor driving the rotating shaft is installed above the cone. The rotating shaft is extended to the bottom of the cone and is then attached to the cone wall with three bars. In this way, vibrations induced by the imperfections of the cone are largely suppressed. A schematic view of this design is depicted in Figure 5, and the dimensions of the cones used are presented in Table I.
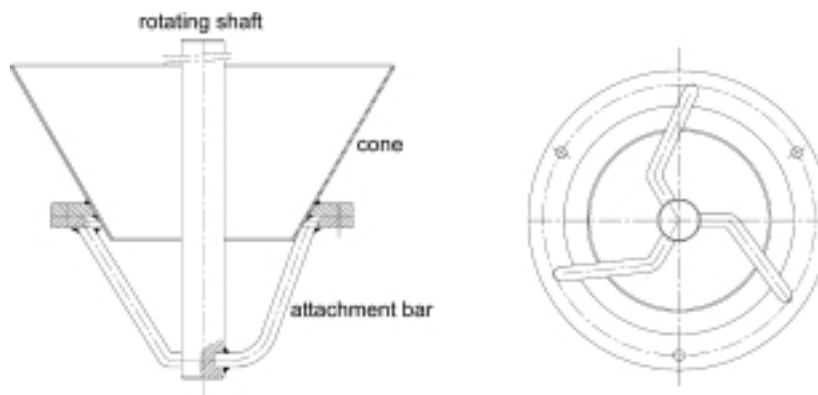

Figure 5.
Rotating cone with attachment bars: side view (left) and bottom view (right)

The liquid used should preferably simulate the gas-solids flow and thus have a density and viscosity of the same order of magnitude as the gas-solids mixture. For comparison, the density of a sand-air mixture with a porosity of ~0.5 is ~1,200 to ~1,300 kg/m^3. Concerning the viscosity, rheological work with a ballotini-air system (Schügerl *et al.*, 1961; Grace, 1977) indicated that at low shear rates Newtonian behaviour can be expected while typical values for the (solid phase shear) viscosity are ~0.5 to ~1.2Pa s. An extensive search for a suitable liquid initially resulted in the application of glycerin which is a highly viscous fluid (1.5Pa s at 1bar and 293K) with a moderately high density (1,260 kg/m^3). The main drawback of glycerin is its hygroscopic behavior towards water in the atmosphere with dramatic effects on its properties and thus on the experimental results. Alternatives for glycerin are paraffin and vegetable oils. Due to the low costs and its availability, much less viscous soy oil is applied in the experiments. The density of the oil is 991kg/m^3 and the dynamic viscosity is 0.04 Pa s at 1bar and 293K.

A simple yet effective arrangement is applied to conduct the experiments. Liquid held in an inner container is transported along the cone wall, falls into a larger outer container and is pumped back to the inner container. In this way the mass flow rate of the liquid is easily measured. The rotating cone is mounted above an inner transparent acrylic container that is placed inside a larger outer container. The motor that drives the cone is assembled above the cone in a table-like arrangement. The liquid contained in the inner container is transported by the cone, is slung against the wall of the outer container and falls to the liquid level in this container. From the outer container, the liquid is pumped back by a gear pump to the inner container via an opening in the wall. The liquid layer thickness is measured with a screw micrometer, that is arranged in such a way that it points perpendicular to the cone wall. The point at which it brushes the liquid layer surface and the point where it brushes the cone wall is measured and the difference is assumed to be equal to the layer thickness.

Although the visual measurement of the point at which the screw micrometer just brushes the liquid layer is not straightforward, the reproducibility of all the measurements of the liquid layer thickness was typically within 2 per cent. From a laboratory analysis of regularly taken samples, the exact density and viscosity at the operating temperatures were

Cone	θ_w °	D_i 10^{-3}m	D_o 10^{-3} m	H 10^{-3} m
A	45.0	150.0	440.0	145.0
B	37.5	150.0	372.5	145.0
C	30.0	150.0	317.4	145.0
a	45.0	50.0	146.8	48.4
b	37.5	50.0	124.3	48.4
c	30.0	50.0	105.9	48.4

Table I.
Dimensions of cones

obtained. A constant liquid temperature was maintained by water-cooling the contents of the outer container. The arrangement of the apparatus is depicted in Figure 6.

2.6 Analytical solutions

2.6.1 Very low angular cone velocities. When the cone rotates at a very low angular frequency, the system can be described as a fluid that resides in a conical container rotating about its own vertical axis. Due to the low rotation velocity, the hydrodynamic character of the flowing liquid shows resemblance with the rotation of a rigid body. This problem is solved along the lines of the solution of a rotating cylinder that rotates at a very low angular frequency presented by Bird *et al.* (1960). The complete solution procedure can be found in Appendix 1 and results in the following set of equations to determine the location of the free surface either as a function of r or θ (for the symbols and dimensionless variables, refer to Appendix 1):

$$r_s = \frac{g\cos\theta}{\Omega^2\sin^2\theta}\left(1 - \sqrt{1 + \frac{2\Omega^2 r_{s,0}}{g}\left(1 - \frac{1}{\cos^2\theta}\right)}\right) \tag{12}$$
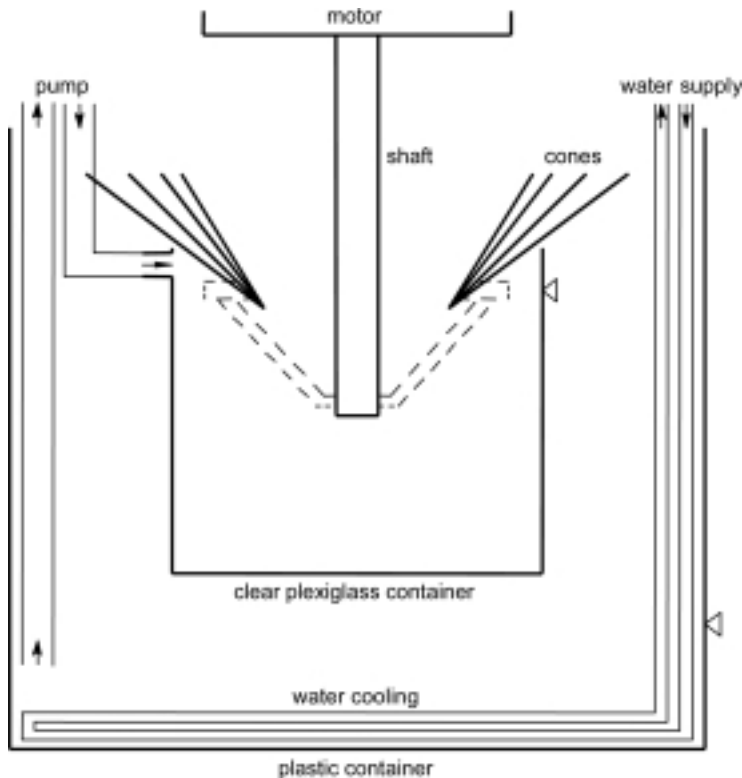

Figure 6.
Arrangement of
experimental apparatus

$$\cos\theta_s = \frac{g}{\Omega^2 r}\left(-1 + \sqrt{1 + \frac{2\Omega^2}{g}\left(\frac{\frac{1}{2}\Omega^2 r^2}{g} + r_{s,0}\right)}\right). \tag{13}$$

The orientation of the free surface boundary is derived by differentiation of the free surface boundary equation (equations (12) and (13)) with respect to θ and r, respectively. This derivation and the resulting lengthy equations will not be presented here. The free surface boundary is oriented along r for

$$\frac{1}{r_s}\frac{\partial r_s}{\partial\theta} > r_s\frac{\partial\theta_s}{\partial r} \tag{14}$$

and along θ otherwise.

2.6.2 Very high angular cone velocities. At high angular frequencies, transport of fluid through the cone prevails, in contrast to the previous situation. This problem has been studied earlier by Bruin (1969) nearly three decades ago but unfortunately his paper contained a number of typographical errors. Therefore, we present here the correct solution, which differs slightly from Bruin's solution. For details, see Appendix 2.

Bruin (1969) introduced a scaled dimensionless rotation frequency number

$$\Omega = \frac{\omega r_o \sin\theta_w}{|v_r|_{r=r_o}} \tag{15}$$

and obtained for very high values of Ω (e.g. 20, recommended by Bruin) the following solution for the different velocities and pressure:

r-velocity component:

$$U = \frac{v_r}{\omega r \sin\theta_w} = \left(\sin\theta_w - \frac{\cos\theta_w}{Fr}\right)\left(\delta^+\sigma - \frac{1}{2}\sigma^2\right) \tag{15a}$$

θ-velocity component:

$$W = \frac{v_\phi}{\omega r \sin\theta_w} = -\frac{1}{3}\left(\sin^2\theta_w - \frac{\sin 2\theta_w}{2Fr}\right)\left(\delta^+\sigma^3 - \frac{1}{4}\sigma^4 - 2(\delta^+)^3\sigma\right) \tag{15b}$$

ϕ-velocity component:

$$V = \frac{v_\theta}{(\nu\omega)^{1/2}} = \left(3\sin^2\theta_w - \frac{\sin 2\theta_w}{Fr}\right)\left(\frac{1}{2}\delta^+\sigma^2 - \frac{1}{6}\sigma^3\right) \tag{15c}$$

pressure:

$$P = \frac{p - p_a}{\rho(\nu\omega)^{1/2}\omega r \sin\theta_w} = \left(\cos\theta_w + \frac{\sin\theta_w}{Fr}\right)(\delta^+ - \sigma) \qquad (15d)$$

with
  r-coordinate:

$$\eta = \frac{r}{r_o} \qquad (16a)$$

θ-coordinate:

$$\sigma = \left(\frac{\omega}{\nu}\right)^{1/2}d \qquad (16b)$$

Froude number:

$$Fr = \frac{\omega^2 r \sin\theta_w}{g} \qquad (16c)$$

The dimensionless film thickness

$$\delta^+ = \left(\frac{\omega}{\nu}\right)^{1/2}d_s \qquad (17)$$

can be derived from the conservation of mass over a cross section of the liquid
film (equations (A2)-(A19))

$$\delta^+ = \sqrt[3]{\frac{3Q_0^+}{\left(\sin\theta_w - \frac{\cos\theta_w}{Fr}\right)}} \qquad (18)$$

with

$$Q_0^+ = \frac{Q_0}{2\pi r^2 \sin^2\theta_w(\nu\omega)^{1/2}}. \qquad (19)$$

2.6.3 Intermediate angular cone velocities. Bruin (1969) also presented the
solutions for intermediate angular cone velocities ($\Omega > 1$).

Bruin first derived expressions for the U and W velocity components, and
subsequently solved for the V velocity component and the pressure P. For
brevity, the solution is presented below while the complete mathematical
procedure can be found in Bruin's paper.

$$U(\eta, \sigma) = \frac{1}{2\sin\theta_w}F(\eta)(\xi_r - \sinh\lambda\sigma\sin\lambda\sigma) \qquad (20a)$$

$$W(\eta, \sigma) = \frac{1}{2 \sin \theta_{\mathrm{w}}} F(\eta)(\xi_i - \cosh \lambda \sigma \cos \lambda \sigma + 1) \qquad (20\mathrm{b})$$

$$V(\eta, \sigma) = \left(\tfrac{3}{2} \sin \theta_{\mathrm{w}} - \frac{\cos \theta_{\mathrm{w}}}{Fr} \right) I_{f,u}(\sigma, \delta^+) + \\ \frac{\eta}{2} \left(\sin \theta_{\mathrm{w}} - \frac{\cos \theta_{\mathrm{w}}}{Fr} \right) X_i(\eta, \delta^+) I_{\xi,r}(\sigma, \delta^+) \qquad (20\mathrm{c})$$

$$P = \frac{1}{2 \sin \theta_{\mathrm{w}}} F(\eta) \left(\frac{2\Theta \sin \theta_{\mathrm{w}}}{\eta} \right) \xi_r - \xi_r(\delta^+)) - \\ (\sinh \lambda \sigma \sin \lambda \sigma - \sinh \lambda \delta^+ \sin \lambda \delta^+) \\ + 2 \cos \theta_{\mathrm{w}} I_{f,w}(\sigma, \delta^+)) + \left(\cos \theta_{\mathrm{w}} + \frac{\sin \theta_{\mathrm{w}}}{Fr} \right) (\delta^+ - \sigma) \qquad (20\mathrm{d})$$

with

$$\lambda = \sqrt{\sin \theta_{\mathrm{w}}} \qquad (21\mathrm{a})$$

$$F(\eta) = \sin \theta_{\mathrm{w}} - \frac{\cos \theta_{\mathrm{w}}}{Fr} \qquad (21\mathrm{b})$$

$$\xi_r = \frac{\sin 2\lambda\delta^+ \sinh \lambda\sigma \cos \lambda\sigma + \sinh 2\lambda\delta^+ \cosh \lambda\sigma \sin \lambda\sigma}{\cosh 2\lambda\delta^+ + \cos 2\lambda\delta^+} \qquad (21\mathrm{c})$$

$$\xi_i = \frac{\sinh 2\lambda\delta^+ \sinh \lambda\sigma \cos \lambda\sigma - \sin 2\lambda\delta^+ \cosh \lambda\sigma \sin \lambda\sigma}{\cosh 2\lambda\delta^+ + \cos 2\lambda\delta^+}. \qquad (21\mathrm{d})$$

The relatively lengthy expressions for $I_{f,u}(\sigma, \delta^+), \Xi(\eta, \delta^+), I_{\xi,r}(\sigma, \delta^+)$ and $I_{f,w}(\sigma, \delta^+)$ are defined in Appendix 3. Finally, the thickness of the film along the cone wall can be computed from

$$F(\eta) \left(\frac{\sinh 2\lambda\delta^+ - \sin 2\lambda\delta^+}{\cosh 2\lambda\delta^+ + \cos 2\lambda\delta^+} \right) = 2 \sin \theta_{\mathrm{w}}(1 + \lambda) Q_0^+. \qquad (22)$$

3. Results and discussion
3.1 Analytic solutions validated by experimental observations
The comparison between the analytical solutions and the experimental observations is presented in Figures 7(a)-(d) in terms of the layer thickness versus the dimensionless cone coordinate η (as defined by equation ((16a)). The value of the parameter Ω, which is a function of the cone dimensions, inlet volumetric flow rate and cone rotation frequency increases from 13.7 in Figure
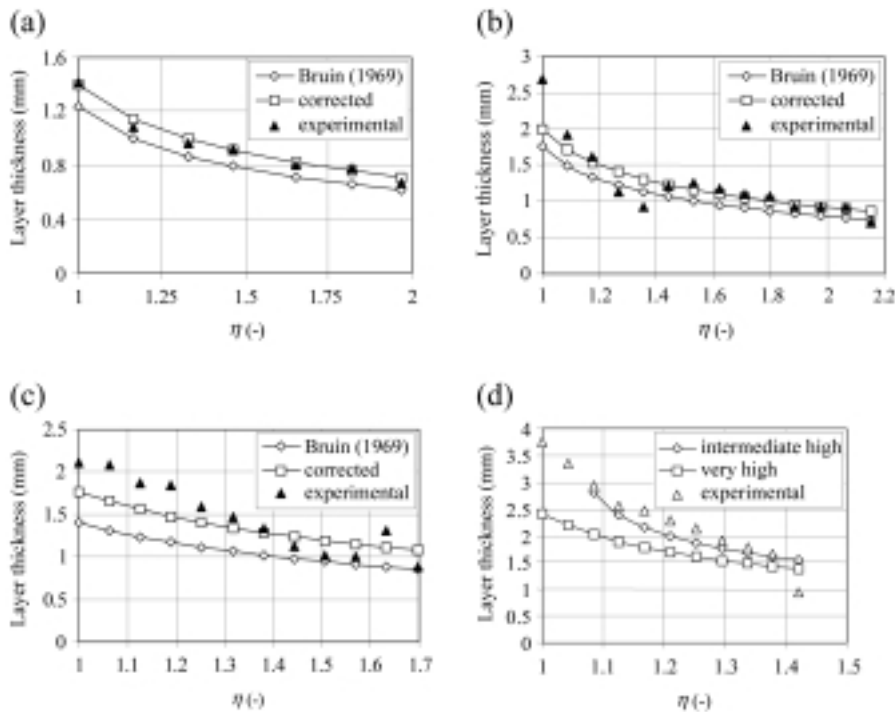
Notes: (a) in the intermediate high angular cone velocity regime at Ω=13.7 (θ_κ=45°, n=4 Hz, r_1=0.0527m, Q_0=31.6 ml/s), (b) in the intermediate high angular cone velocity regime at Ω=20.2 (θ_κ=45°, n=2 Hz, r_1=0.170m, Q_0=115 ml/s), (c) in the very high angular cone velocity regime at Ω=31.0 (θ_κ=30°, n=2.5 Hz, r_1=0.202 m, Q_0=115 ml/s), and (d) in the intermediate high and very high cone angular velocity regime at Ω=49.4 (θ_κ=25°, n=2.5 Hz, r_1=0.237 m, Q_0=115 ml/s).

Figure 7.
Comparison between
analytical solutions and
experiments

7(a) to 49.3 in Figure 7(d). The comparison in the intermediate high angular frequency regime is shown in Figures 7(a) and (b), while the solution pertaining to the very high angular frequency regime is presented in Figures 7(c) and (d). Because of the implicit expression for the layer thickness in the intermediate high regime (equation (22)), this parameter was computed numerically using the Newton-Rapson technique (Press *et al.*, 1986). For comparison, the solution of Bruin (1969) was also added to Figures 7(a)-(c) to show the differences between his solution and the solution as presented in this work. The solution of Bruin (1969) underestimates the thickness of the film.

A physical situation, which should belong to the very high angular frequency regime of Bruin (1969) is shown in Figure 7(d). However, it is clear that the computed layer thickness is too low in comparison with the experimentally determined layer thicknesses. The intermediate high solution, which is also presented in Figure 7(d), shows much better agreement; therefore, it seems that the criterion of Bruin (1969) to discriminate between the two

hydrodynamic regimes ("intermediate high" and "very high" angular cone velocity) by using a value of $\Omega = 20$, is in some situations not adequate. To clarify the differences between the solutions in the intermediate high angular cone velocity regime and in the very high regime, the layer thickness, computed from equations (16a) and (18), is plotted in Figure 8(a) and (b) as a function of Ω for two different values of r. It can be concluded from both figures that a value of $\Omega = 40$ is a better criterion than $\Omega = 20$ to distinguish between the two hydrodynamic regimes. The differences in layer thickness between the very high and intermediate high angular frequency regime are less than 5 per cent for $\Omega > 40$.
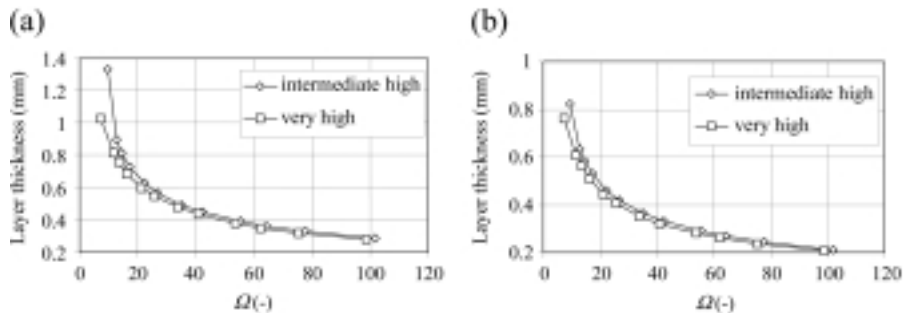
A remarkable feature in the experimental data points shown in Figure 8 is the low value of the film thickness at $\eta = 1.26$. Probably this is caused by a flow outlet effect. The direction of the r-component of the velocity of the film is changed immediately after reaching the upper edge of the cone from along the cone wall to an outward oriented direction due to the strong centrifugal forces. It is likely that the very high speed of the liquid just outside the upper edge of the cone drags liquid that is still inside the cone resulting in higher velocities. Consequently, this results in a lower film thickness.

3.2 Numerical results validated with analytical solutions

The numerical results were validated thoroughly using analytical solutions obtained for flow between two concentric spheres (Bird *et al.*, 1960), and cone and plate viscometers (Bird *et al.*, 1960). The agreement between the results obtained with the numerical model and the analytical solutions was within 1 per cent.

Subsequently, approximate analytical solutions for flow in rotating cones, based on the work of Bruin (1969), were used to validate the numerical results. The average liquid residence time τ was used as a criterion. It is a function of the mass flow rate, the density and the volumetric hold-up, and can be computed from

$$\tau = \frac{\rho \dot{M}}{V}.$$ (23)

Figure 8.
Difference between intermediate high and very high angular frequency

Notes: (θ=25°, n=2.5 Hz, r_i=0.237 m, Q_0=115 ml/s): (a) at inlet $r=r_i$, and (b) at $r=1.5\,r_i$

The volumetric hold-up (i.e. the volume of the liquid layer) V is a function of the integrated layer thickness with respect to the relevant coordinates

$$V = \int\limits_{\phi=0}^{2\pi} \int\limits_{\theta=\theta_w}^{\theta_d} \int\limits_{r=r_i}^{r_o} r^2 \sin\theta \, dr \, d\theta \, d\phi \qquad (24)$$

By integrating in the ϕ-direction and substituting the film thickness $d(r)$ that is equal to $rd\theta$ into equation (24), it is rewritten to

$$V = 2\pi \int\limits_{r_i}^{r_o} d(r) \, r \sin\theta \, dr \qquad (25)$$

The parity plot of the residence times that were simulated numerically and obtained from the approximate analytical solution is presented in Figure 9.

It appears that some discrepancies, sometimes up to 20 per cent, exist between the numerical results and the analytical solution. These discrepancies are due to imperfections of the numerical model that are especially profound for thin films. To explain this, a typical example of the computed film thickness as a function of the radial coordinate is plotted in Figure 10. The film thickness shows some peaks, which are not feasible from a physical point of view. Thorough checking of the computer algorithms revealed that these peaks are due to an inaccurate approximation of the pressure calculation at the surface of the very thin flowing layer, which is sometimes only a few tenths of a mm thick (see for example Figure 10). The film thickness peaks occur, from a numerical point of view, at transition points where the fluid layer thickness, expressed in terms of number of grid cells in the θ-direction, changes. The influence of these peaks on the residence time will be more severe for thinner layers that occuring at, e.g. high rotational speeds. This effect can be suppressed by reducing the number of transition points, which is equivalent to reducing the number of
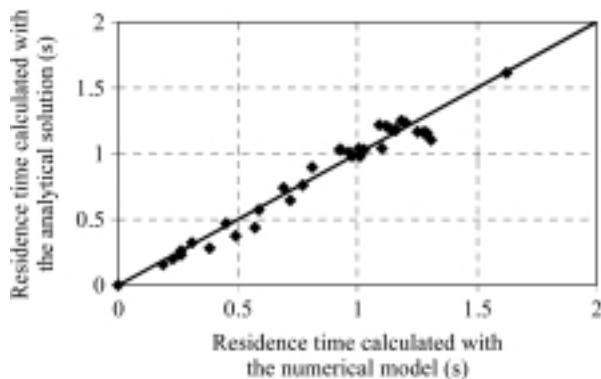
Figure 9.
Parity plot of the residence time of fluid elements on the cone wall as calculated with the numerical model and the analytical solution

Notes: $r_i=0.15$ m, $r_o=0.35$ m, $\phi_m=0.1$ kg/s, $\rho=991$ kg/m^3, $\mu=0.04$ Pas

computational cells in the θ-direction for a given physical situation. In addition, the spherical coordinates that are used to describe this system complicate matters considerably: for increasing r-coordinate, the width of the numerical grid cells in the θ-direction increases. At the same time, the layer thickness decreases for increasing r-coordinate. As a result, it becomes increasingly difficult to capture the layer within a sufficient number of grid cells, without creating instability problems (equations (10) and (11)) at the cone inlet. A more detailed analysis of this problem is presented in Janse *et al.* (2000).

3.3 Numerical simulations

Numerical simulations have been performed to investigate the influence of the cone top angle, rotation frequency and characteristic cone dimensions on the average residence time on the cone wall. During the simulations, the length of the cone wall was fixed ($r_i = 0.15$m, $r_o = 0.35$m), together with the physical properties of the medium, which were already presented in the previous section. The influence of the cone rotation speed and mass flow rate on the experimentally determined average residence time of fluid elements is presented in Figure 11.

As can be expected, the residence time decreases with increasing cone rotation frequency. The influence is highest at the lower frequencies, while at the higher frequencies the cone rotation has a limited influence. It seems that at

Figure 10.
Typical example of the film thickness as computed from the analytical solutions versus the radial coordinate
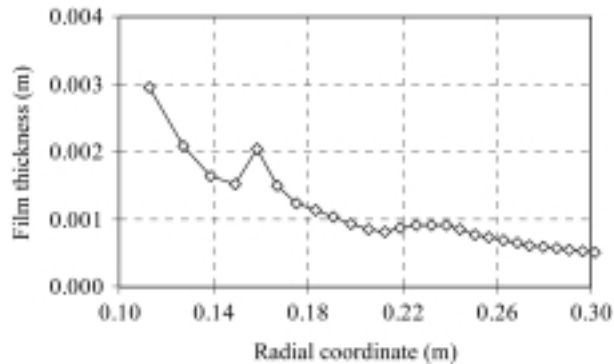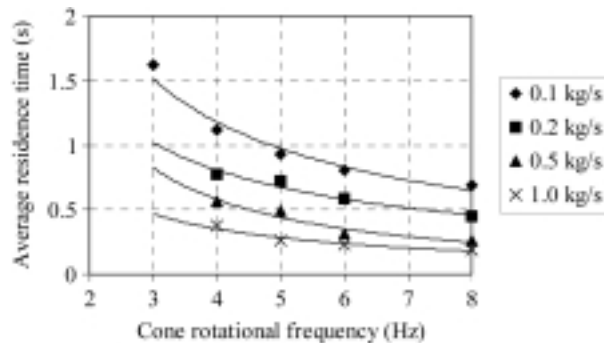

Figure 11.
Influence of the cone rotation frequency on the average residence time of fluid elements on the cone wall derived from experimental film thickness and equations (14)-(16) ($\theta_w = 45°$)

the higher frequencies (and thus higher centrifugal forces) the influence of the no-slip boundary condition at the wall on the thinner films (with increasing cone speed) is becoming more pronounced. Furthermore, the effect that an increase in mass flow rate induces also a decrease in average residence time, can be explained by the fact that due to continuity requirements an increase in mass flow rate can only be enforced by an increase of the fluid inlet velocity. In other words, because the calculation domain in the θ-direction is not changed at varying mass flow rate, the inlet velocity in r-direction varies also. We have chosen for the approach of constant layer thickness at the inlet (implying a changing boundary condition for the liquid velocity), instead of constant inlet velocity; in our experimental work we imposed a mass flow rate to the cone wall. To mimic the simulations as much as possible the situation that a higher mass flow rate is generated by increasing the submersion depth of the cone and in this way force more liquid to the cone inner side, the layer thickness is kept constant near the inlet.

Very important for a reliable cone design is the cone angle, because this parameter not only influences the residence time on the cone wall, but also influences the overall size of the equipment and the overall strength of the rotating parts (i.e. the type of material). The effect of the cone angle on the average residence time is depicted in Figure 12 for a cone with a half top angle of $45°$ and a cone rotation frequency of 4Hz and 5Hz. This figure shows clearly that the cone top angle has a minor influence on the average residence time. At a cone frequency of 4Hz, a small increase can be observed but for a cone rotation frequency of 5Hz, the residence time nearly remains constant at approximately one second. Therefore, the conclusion is justified that the cone angle cannot be used effectively to change the average residence time of fluid elements on the cone wall.

The influence of the length of the cone wall was also investigated to obtain insight in the scalability of the cone. The corresponding results as computed with the numerical model are presented in Figure 13.

It can be observed that, in a good approximation, the cumulative average residence time of fluid elements on the cone wall is linearly dependent on the length of the cone wall (i.e. r). Thus, when higher residence times are required
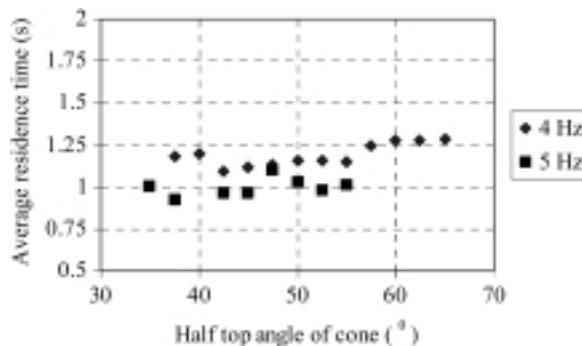

Figure 12.
Influence of the cone top angle on the average residence time of fluid elements on the cone wall as computed with numerical model (n = 4Hz, ϕ_{m} = 0.1kg/s)

due to for instance longer required processing times, it is useful to use a larger cone. Of course, the size is limited by mechanical considerations.

As a concluding remark it can be stated that even with these small scale cones of characteristic dimension of ~10cm to ~30cm, throughputs are possible of more than 1kg/s without requiring very high cone rotation frequencies. Besides, because the film thickness is very small (up to a few mm), the actual reactor volume can be very low. So from this point of view this novel reactor type can be considered as a high intensity reactor. However, it must be emphasized that for processes that require or produce heat, also heat transfer considerations should be taken into account before judging a rotating cone as a high intensity reactor.

4. Conclusions

Numerical simulations have been developed for the description of liquid films flowing over the conical surface of a rotating cone. The principal objective was to compute the liquid residence times and to investigate the most important parameters influencing it. The simulations were validated by comparing its results with those obtained from experimental observation and approximate analytical solutions of the model equations. Due to inaccuracies in pressure interpolations near the free surface required in the VOF model, deviations of up to 20 per cent were obtained. However, the numerical simulation has the flexibility of incorporating complex changing variables and may be improved by the introduction of a more refined algorithm. On the other hand, it turned out that the combination of the decreasing layer thickness and the increasing size of the numerical grid cells with increasing radial cone coordinate hampers the numerical simulation of this system.

The velocity and pressure distributions in a liquid film flowing over the conical surface of the rotating cone reactor have been derived by solving the simplified conservation equations for mass and momentum analytically. To this end, the range of cone rotation frequencies has been classified into three different hydrodynamic regimes: very slow, intermediate and very high angular cone velocities.
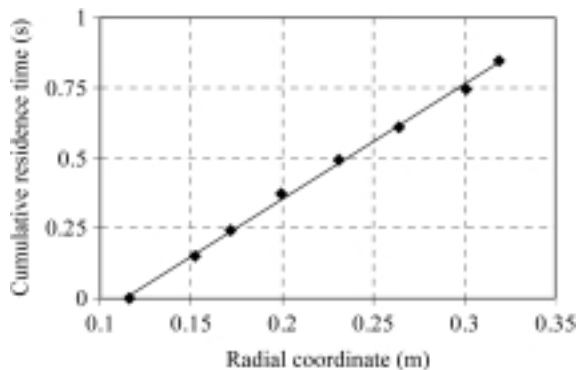

Figure 13.
Influence of the length of the cone wall on the average residence time of fluid elements
($\theta_w = 45°$, $\phi_m = 0.1$kg/s, $n = 4$Hz)

The numerical simulations have been validated thoroughly by comparing the computed thickness of the flowing film along the conical surface of the reactor wall with the experimentally determined thickness. The agreement between the simulations and the experiment was satisfactory.

The numerical simulations showed that the cone angle was of minor influence on the residence time, while both the length of the cone wall and the cone rotation frequency have a strong influence. Moreover, the simulations revealed the enormous transport and pumping capacity of the rotating cone. Even with the small-scale cones employed in this work, throughputs exceeding 1kg/s could be achieved.

References

Bird, R.B., Stewart, W.E. and Lightfoot, E.N. (1960), *Transport Phenomena*, John Wiley & Sons, New York, NY.

Bruin, S. (1969), "Velocity distributions in a liquid film flowing over a rotating conical surface", *Chem. Eng. Sci.*, Vol. 25, p. 1647.

Buckingham, E. (1914), "On physically similar systems; illustrations of the use of dimensional equations", *Phys. Rev.*, Vol. 4, p. 345

Grace, J.R. (1977), "The viscosity of fluidized beds", *Can. J. Chem. Eng.*, Vol. 48, p. 30.

Hinze, J.O. and Milborn, H. (1950), "Atomization of liquids by means of a rotating cup", *J. Applied Mech.*, Vol. 145.

Hirt, C.W. and Nichols, B.D. (1981), "Volume of fluid (VOF) method for the dynamics of free boundaries", *J. Comp. Phys.*, Vol. 39, p. 201.

Hoomans, B.P.B., Kuipers, J.A.M. and van Swaaij, W.P.M. (2000), "Granular dynamics simulation of segregation phenomena in bubbling gas-fluidized beds", *Powder Technol.*, Vol. 109, p. 41.

Hoomans, B.P.B., Kuipers, J.A.M., Briels, W.J. and van Swaaij, W.P.M. (1996), "Discrete particle simulation of bubble and slug formation in a two-dimensional gas-fluidized bed: a hard-sphere approach", *Chem. Eng. Sci.*, Vol. 51, p. 99.

Janse, A.M.C. (1998), "A heat integrated rotating cone reactor system for flash pyrolysis of biomass", PhD Thesis, Twente University, Enschede.

Janse, A.M.C., Dijk, P.E. and Kuipers, J.A.M. (2000), "The volume of fluid method in spherical coordinates", *Inter. J. Num. Meth. Heat Fluid Flow*, Vol. 10, p. 654.

Janse, A.M.C., Biesheuvel, P.M., Prins, W. and van Swaaij, W.P.M. (1999), "A novel interconnected fluidized bed for the combined flash pyrolysis of biomass and combustion of char", *Chem. Eng. J.*, Vol. 75, p. 121.

Kuipers, J.A.M., van Duin, K.J., van Beckum, F.P.H. and van Swaaij, W.P.M. (1992), "A numerical model of gas-fluidized beds", *Chem. Eng. Sci.*, Vol. 47, p. 1913.

Nichols, B.D., Hirt, C.W. and Hotchkiss, R.S. (1980), "SOLA-VOF: a solution algorithm for transient fluid flow with multiple free boundaries", *Los Alamos Scientific Laboratory Report LA-8355*, Los Alamos, NM.

Press, W.H., Flannery, B.P., Teukolsky, S.A. and Vetterling, W.T. (1986), *Numerical Recipes*, Cambridge University Press, Cambridge.

Schügerl, K., Merz, M. and Fetting, F. (1961), "Rheologische Eigenschaften von gasdurchströmten Fliessbettsystemen", *Chem. Eng. Sci.*, Vol. 15, p. 1.

Wagenaar, B.M., Prins, W. and van Swaaij, W.P.M. (1994a), "Pyrolysis of biomass in the rotating cone reactor", *Chem. Eng. Sci.*, Vol. 49, p. 5109.

Wagenaar, B.M., Kuipers, J.A.M. and van Swaaij, W.P.M. (1994b), "Particle dynamics and gas phase hydrodynamics in a rotating cone reactor", *Chem. Eng. Sci.*, Vol. 47, p. 927.

Westerhout, R.W.J., Waanders J., Kuipers, J.A.M. and van Swaaij, W.P.M. (1998a), "Recycling of polyethene and polypropene in a novel bench-scale rotating cone reactor by high-temperature pyrolysis", *Ind. Eng. Chem. Res.*, Vol. 37, p. 2293.

Westerhout, R.W.J., Waanders, J., Kuipers, J.A.M. and van Swaaij, W.P.M. (1998b), "Development of a continuous rotating cone reactor pilot plant for the pyrolysis of polyethene and polypropene", *Ind. Eng. Chem. Res.*, Vol. 37, p. 2316.

Appendix 1. Analytical solution at very low angular cone velocities

As stated in section 2.6.1, when the cone rotates at very low angular frequency, the system can be described as a fluid that resides in a conical container rotating about its own vertical axis. Due to the low rotation velocity, the hydrodynamic character of the flowing liquid shows resemblance with the rotation of a rigid body. This problem is solved along the lines of the solution of a rotating cylinder that rotates at a very low angular frequency presented by Bird *et al.* (1960).

Besides the assumptions mentioned earlier in section 2.6.1, the r- and θ- velocity components are assumed to be negligible with $v_r = 0$ and $v_\theta = 0$. When these assumptions are applied to the partial differential mass conservation equation (4), it reduces to a trivial equation. The r-, θ- and ϕ-velocity components of the momentum conservation equation (5) (Bird *et al.*, 1960) are thus simplified to

$$-\rho \frac{v_\phi^2}{r} + \frac{\partial p}{\partial r} + \rho g \cos \theta = 0 \tag{A1-1}$$

$$-\rho \frac{\cot \theta v_\phi^2}{r} + \frac{1}{r} \frac{\partial p}{\partial \theta} - \rho g \sin \theta = 0 \tag{A1-2}$$

$$-\frac{\mu}{r^2} \frac{\partial}{\partial r} \left(r^2 \frac{\partial v_\phi}{\partial r} \right) - \frac{\mu}{r^2} \frac{\partial}{\partial \theta} \left(\frac{1}{\sin \theta} \frac{\partial (\sin \theta v_\phi)}{\partial \theta} \right) = 0 \tag{A1-3}$$

The boundary conditions defining the solution of these equations are as follows. At the central symmetry line, the ϕ-velocity component must have a non-zero value. At the rotating cone wall, the ϕ-velocity component is equal to the rotation velocity of the wall (no-slip condition) which rotates at a fixed angular frequency. The pressure at the free surface boundary located at the central symmetry line is equal to the atmospheric pressure. The boundary conditions are:

(1)   the central symmetry line for $\theta = 0$ with $v_\theta \neq 0$;

(2)   the cone wall for $\theta = \theta_w$ with $v_\phi = \Omega r \sin \theta_w$; and

(3)   the free surface at the central symmetry line for $r = r_{s,0}$ and $\theta = 0$ with $p = p_a$.

As mentioned before, it is postulated that the fluid rotates as if it were a rigid body. Its ϕ velocity component is thus given by

$$v_\phi = W r \sin \theta \tag{A1-4}$$

This equation can be rewritten into the dimensionless form as

$$\frac{v_\phi}{\Omega r_{s,0}} = \frac{r \sin \theta}{r_{s,0}}. \tag{A1-5}$$

If this expression for the ϕ-velocity component is substituted into equation A1-1a, the equation for the pressure gradient in radial direction is given by

$$\frac{\partial p}{\partial r} = \rho\Omega^2 r \sin^2\theta - \rho g \cos\theta \qquad (A1\text{–}6)$$

which can be integrated to yield

$$p = \tfrac{1}{2}\rho\Omega^2 r^2 \sin^2\theta - \rho g r \cos\theta + c_\theta(\theta), \qquad (A1\text{–}7)$$

where $c_\theta(\theta)$ is an integration constant depending only on θ. Substitution of this expression into equation A1-2 and subsequent integration with respect to θ yields

$$p = \tfrac{1}{2}\rho\Omega^2 r^2 \sin^2\theta - \rho g r \cos\theta + c_r(r), \qquad (A1\text{–}8)$$

where $c_r(r)$ is an integration constant depending only on r. The equation for the pressure distribution can now be obtained by combination of equations A1-7 and A1-8, and subsequent enforcement of the boundary conditions

$$p = p_a + \tfrac{1}{2}\rho\Omega^2 r^2 \sin^2\theta + \rho g \left(r_{s,0} - r\cos\theta\right). \qquad (A1\text{–}9)$$

This expression can be transformed into the following two equivalent dimensionless forms

$$\frac{p - p_a}{\rho g r_{s,0}} = \frac{\tfrac{1}{2}\Omega^2 r^2 \sin^2\theta}{g r_{s,0}} + 1 - \frac{r\cos\theta}{r_{s,0}} \qquad (A1\text{–}10a)$$

$$\frac{p - p_a}{\rho\Omega^2 r_{s,0}^2} = \tfrac{1}{2}\left(\frac{r\sin\theta}{r_{s,0}}\right)^2 + \frac{g}{\Omega^2 r_{s,0}}\left(1 - \frac{r\cos\theta}{r_{s,0}}\right). \qquad (A1\text{–}10b)$$

The location of the free surface boundary, either as a function of r or θ, can now be easily obtained from the known free surface pressure boundary condition $p = p_a$ which yields the following expressions for the location of the free surface

$$r_s = \frac{g\cos\theta}{\Omega^2 \sin^2\theta}\left(1 - \sqrt{1 + \frac{2\Omega^2 r_{s,0}}{g}\left(1 - \frac{1}{\cos^2\theta}\right)}\right) \qquad (A1\text{–}11a)$$

$$\cos\theta_s = \frac{g}{\Omega^2 r}\left(-1 + \sqrt{1 + \frac{2\Omega^2}{g}\left(\frac{\tfrac{1}{2}\Omega^2 r^2}{g} + r_{s,0}\right)}\right). \qquad (A1\text{–}11b)$$

Appendix 2. Analytical solution at very high angular cone velocities

At high angular frequencies, transport of fluid through the cone prevails, in contrast to the previous situation. This problem has been studied earlier by Bruin (1969) nearly three decades ago but unfortunately his paper contained a number of typographical errors. Therefore, we will present the solution again here.

At very high angular cone velocities, the fluid layer thickness is very small with respect to the characteristic dimension of the cone

$$\frac{d_o}{r_o} << 1, \qquad (A2\text{–}1)$$

where d_o represents the outer diameter of the cone. In addition to the basic assumptions mentioned earlier, it is assumed that, as a result of the very thin fluid layer, the θ-velocity component is negligible compared to the r- and ϕ-velocity components with $v_\theta << v_r$ and $v_\theta << v_\phi$. Further, it is assumed that the pressure gradient in radial direction is negligible compared to the other terms in the momentum equation in radial direction

$$\frac{\partial p}{\partial r} = 0. \tag{A2-2}$$

In the thin film approximation, the kinematic viscosity possesses a very low value, which allows the following assumptions

$$v_r >> \frac{4\nu}{r}, \ v_\theta >> \frac{\nu \cot \theta}{r}, \ v_\phi >> \frac{2\nu}{r} \tag{A2-3}$$

$$v_r >> \frac{2\nu}{r}, \ v_\theta >> \frac{\nu(\cot^2 \theta + 1)}{r}. \tag{A2-4}$$

Furthermore, it can be argued that due to the high gradients of the radial velocity component in the θ-direction the following assumption is allowed:

$$\frac{\partial^2 v_r}{\partial r^2} << \frac{\partial^2 v_r}{\partial \theta^2}. \tag{A2-5}$$

The first order derivative of the radial velocity component with respect to θ is larger than all other first and second order derivatives of the θ-component

$$\text{first and second order derivatives of } v_\theta << \frac{\partial v_r}{\partial \theta}. \tag{A2-6}$$

The second order derivative of the ϕ velocity component v_ϕ with respect to r is negligible compared to its second order derivative with respect to θ

$$\frac{\partial^2 v_\phi}{\partial r^2} << \frac{\partial^2 v_\phi}{\partial \theta^2}. \tag{A2-7}$$

Furthermore, it can be proven that (as a good approximation) the following term in the ϕ-momentum conservation equation can be neglected

$$\frac{\nu \omega \sin \theta}{r} = 0. \tag{A2-8}$$

Finally, because of the small film thickness, the assumption is made that the geometrical functions are not a function of θ. They are assumed to be equal to the corresponding geometrical functions of θ_w, which represents half the top angle of the cone.

When the assumptions mentioned above are applied to the mass and momentum equations (4) and (5), the following simplified set of equations is obtained

continuity:

$$\frac{\partial v_r}{\partial r} + \frac{1}{r}\frac{\partial v_\theta}{\partial \theta} + \frac{2v_r}{r} = 0 \tag{A2-9a}$$

r-momentum:

$$-\frac{\nu}{r^2}\frac{\partial^2 v_r}{\partial \theta^2} + v_r\frac{\partial v_r}{\partial r} + \frac{v_\theta}{r}\frac{\partial v_r}{\partial \theta} - \frac{v_\phi^2}{r} + g\cos \theta = 0 \tag{A2-9b}$$

θ-momentum:

$$\frac{2\nu}{r^2}\frac{\partial v_\mathrm{r}}{\partial \theta} - \frac{1}{\rho r}\frac{\partial p}{\partial \theta} - \frac{v_\phi^2 \cot \theta}{r} - g\sin \theta = 0 \tag{A2-9c}$$

ϕ-momentum:

$$-\frac{\nu}{r^2}\frac{\partial^2 v_\phi}{\partial\theta^2} + v_r\frac{\partial v_\phi}{\partial r} + \frac{v_\theta}{r}\frac{\partial v_\phi}{\partial\theta} + \frac{v_r v_\phi}{r} = 0. \tag{A2-9d}$$

The corresponding boundary conditions are:

(1) at the cone wall for $r_i < r < r_o$ and $\theta = \theta_w$ with $v_r = v_\theta = 0$ and $v_\phi = \omega r\sin\theta$;

(2) at the fluid surface for $r_i < r < r_o$ and $\theta = \theta_w$-d with $\partial v_r/\partial\theta = 0$, $\partial v_\phi/\partial\theta = \partial(\omega r\sin\theta)/\partial\theta$ and $p = p_a$; and

(3) at the inlet for $r \geq -r_i$ with $2\pi r^2 \int_{\theta=0}^{\theta_w-d} v_r\sin\theta d\theta = Q_0$.

A new coordinate d is defined as the distance perpendicular to the cone wall with $-\partial d = r\partial\theta$. For convenience, Bruin (1969) defined the following dimensionless parameters:

r-velocity component:

$$U = \frac{v_r}{\omega r\sin\theta_w} \tag{A2-10a}$$

θ-velocity component:

$$V = \frac{v_\theta}{(\nu\omega)^{1/2}} \tag{A2-10b}$$

ϕ-velocity component:

$$W = \frac{v_\phi}{\omega r\sin\theta_w} \tag{A2-10c}$$

pressure:

$$P = \frac{p - p_a}{\rho(\nu\omega)^{1/2}\omega r\sin\theta_w} \tag{A2-10d}$$

r-coordinate:

$$\eta = \frac{r}{r_o} \tag{A2-10e}$$

θ-coordinate:

$$\sigma = \left(\frac{\omega}{\nu}\right)^{1/2}d. \tag{A2-10f}$$

Further, the Froude number Fr is defined by equation (16a), and the following dimensionless numbers were introduced

$$\Theta = \left(\frac{\nu}{\omega}\right)^{1/2}\frac{1}{r_o\sin\theta_w} \tag{A2-11a}$$

$$Q_0^+ = \frac{Q_0}{2\pi r^2\sin^2\theta_w(\nu\omega)^{1/2}}. \tag{A2-11b}$$

Additionally, a scaled dimensionless rotation frequency number Ω was introduced

$$W = \frac{\omega r_o\sin\theta_w}{|v_r|_{r=r_o}} \tag{A2-12}$$

In this equation, the term $|v_r|_{r=r_o}|$ represents the velocity in the *r*-direction averaged over the entire cross section of the layer thickness. Combination of equations (A2-10a-c) with equation (A2-12) results in the following scaled dimensionless velocities

$$\hat{U} \equiv \frac{v_r}{|v_r|_{r=r_o}|} = \Omega\eta U \qquad (A2\text{--}13a)$$

$$\hat{V} \equiv \frac{v_\theta}{|v_r|_{r=r_o}|} = \left(\frac{\nu}{\omega}\right)^{1/2} \frac{1}{r_o \sin\theta_w}\eta V = Q\eta V \qquad (A2\text{--}13b)$$

$$\hat{W} \equiv \frac{v_\phi}{|v_r|_{r=r_o}|} = \Omega\eta W. \qquad (A2\text{--}13c)$$

By substituting these scaled dimensionless variables into the set of conservation equations for mass and momentum (equations (A2-9a-d)), the following set of dimensionless mass and momentum conservation equations is obtained

$$\eta\frac{\partial\partial\hat{U}}{\partial\eta} - \frac{\eta}{Q\sin\theta_w}\frac{\partial\hat{V}}{\partial\sigma} + 2\hat{U} = 0 \qquad (A2\text{--}14a)$$

$$\frac{\eta\Omega}{\sin\theta_w}\frac{\partial^2\hat{U}}{\partial\sigma^2} + \eta\hat{U}\frac{\partial\hat{U}}{\partial\eta} - \frac{\eta\hat{V}}{Q\sin\theta_w}\frac{\partial\hat{U}}{\partial\sigma} - \eta^2\Omega^2 + 2\eta\Omega\hat{W} - \hat{W}^2 + \frac{\eta^2\Omega^2\cot\theta_w}{Fr} = 0 \quad (A2\text{--}14b)$$

$$2Q\Omega\tan\theta_w\frac{\partial\hat{U}}{\partial\sigma} + \eta^2\Omega^2\frac{1}{\cos\theta_w}\frac{\partial P}{\partial\sigma} - \eta^2\Omega^2 + 2\eta\Omega\hat{W} - \hat{W}^2 - \frac{\eta^2\ \Omega^2\tan\theta_w}{Fr} = 0 \quad (A2\text{--}14c)$$

$$\frac{\eta\Omega}{\sin\theta_w}\frac{\partial^2\hat{W}}{\partial\sigma^2} - \eta\hat{U}\frac{\partial\hat{U}}{\partial\eta} + \frac{\eta\hat{V}}{Q\sin\theta_w}\frac{\partial\hat{W}}{\partial\sigma} - \hat{W}\hat{U} + 2\eta\Omega\hat{U} = 0, \qquad (A2\text{--}14d)$$

with the following scaled dimensionless boundary conditions: for the no-slip condition on the wall

$$\eta \geq 1 \ \wedge \ \sigma = 0 \ \Rightarrow \ \hat{U} = 0 \ \wedge \ \hat{V} = 0 \ \wedge \ \hat{W} = 0, \qquad (A2\text{--}15)$$

for the free-slip condition at the surface of the liquid

$$r \geq 1 \ \wedge \ \sigma = \delta^+ \ \Rightarrow \ \frac{\partial\hat{U}}{\partial\sigma} = 0 \ \wedge \ \frac{\partial\hat{W}}{\partial\sigma} = 0 \ \wedge \ P = 0 \qquad (A2\text{--}16)$$

and for the mass conservation

$$\eta \geq 1 \ \ \Rightarrow \ \ \int_{\sigma=0}^{\delta^+} \hat{U}d\sigma = \eta\Omega Q_0^+. \qquad (A2\text{--}17)$$

Bruin (1969) argued that at very high cone velocities, corresponding to the condition $\Omega >> 1$, terms containing Ω^2 tend to dominate with respect to the other terms in equations (A2-14a-d). He considered a value of 20 as sufficiently high to ascertain this approximation. The set of equations can then be further simplified to (in terms of *U, V, W* and *P*)

$$\eta\frac{\partial U}{\partial\eta} - \frac{1}{\sin\theta_w}\frac{\partial V}{\partial\sigma} + 3U = 0 \qquad (A2\text{--}18a)$$

$$-\frac{1}{\sin\theta_{\mathrm{w}}}\frac{\partial^2 U}{\partial\sigma^2} - 1 + \frac{\cot\theta_{\mathrm{w}}}{Fr} = 0 \tag{A2–18b}$$

$$-\frac{1}{\cos\theta_{\mathrm{w}}}\theta_{\mathrm{w}}\frac{\partial P}{\partial\sigma} - 1 - \frac{\tan\theta_{\mathrm{w}}}{Fr} = 0 \tag{A2–18c}$$

$$\frac{1}{\sin\theta_{\mathrm{w}}}\frac{\partial^2 W}{\partial\sigma^2} + 2U = 0 \tag{A2–18d}$$

Equations (A2-18a-d) are solved by simple integration. By applying the corresponding boundary conditions (equations (A2-15) and (A2-16)), the following approximate analytical solutions, valid for very high angular cone velocities (i.e. $\Omega \gg 1$), are obtained:

r-velocity component:

$$U(\eta,\sigma) = \left(\sin\theta_{\mathrm{w}} - \frac{\cos\theta_{\mathrm{w}}}{Fr}\right)(\delta^+\sigma - \tfrac{1}{2}\sigma^2) \tag{A2–19a}$$

θ-velocity component:

$$W(\eta,\sigma) = -\tfrac{1}{3}\left(\sin^2\theta_{\mathrm{w}} - \frac{\sin 2\theta_{\mathrm{w}}}{2Fr}\right)(\delta^+\sigma^3 - \tfrac{1}{4}\sigma^4 - 2(\delta^+)^3\sigma) \tag{A2–19b}$$

ϕ-velocity component:

$$V(\eta,\sigma) = \left(3\sin^2\theta_{\mathrm{w}} - \frac{\sin 2\theta_{\mathrm{w}}}{Fr}\right)(\tfrac{1}{2}\delta^+\sigma^2 - \tfrac{1}{6}\sigma^3) \tag{A2–19c}$$

pressure:

$$P(\eta,\sigma) = \left(\cos\theta_{\mathrm{w}} + \frac{\sin\theta_{\mathrm{w}}}{Fr}\right))\delta^+ - \sigma). \tag{A2–19d}$$

The dimensionless film thickness

$$\delta^+ = \left(\frac{\omega}{\nu}\right)^{1/2}d_{\mathrm{s}} \tag{A2–20}$$

can be derived from the conservation of mass over a cross section of the liquid film (equation (A2-17))

$$\delta^+ = \sqrt[3]{\frac{3Q_0^+}{\left(\sin\theta_{\mathrm{w}} - \frac{\cos\theta_{\mathrm{w}}}{Fr}\right)}}. \tag{A2–21}$$

This solution presented above for the film thickness differs slightly from the solution as presented by Bruin (1969).

Appendix 3. Expressions

$$I_{f,u}(\sigma,\delta^+)$$
$$= \frac{1}{1+\lambda}\frac{\sin 2\lambda\delta^+(\cosh\lambda\sigma\cos\lambda\sigma + \sinh\lambda\sigma\sin\lambda\sigma) + \sinh 2\delta^+(\sinh\lambda\sigma\sin\lambda\sigma - \cosh\lambda\sigma\cos\lambda\sigma)}{\cosh 2\lambda\delta^+ + \cos 2\lambda\delta^+}$$
$$+ \frac{1}{1+\lambda}(\sinh\lambda\sigma\cos\lambda\sigma - \cosh\lambda\sigma\sin\lambda\sigma)$$

$$\tag{A3–1}$$

$$\Xi(\eta,\delta^+) = \frac{\frac{\partial F(\eta)}{\partial \eta}\left(\frac{\sinh 2\lambda\delta^+ - \sin 2\lambda\delta^+}{\cosh 2\lambda\delta^+ + \cos 2\lambda\delta^+}\right)}{2\lambda F(\eta)\left(\frac{\cosh 2\lambda\delta^+ - \cos 2\lambda\delta^+}{\cosh 2\lambda\delta^+ + \cos 2\lambda\delta^+} - \left(\frac{\sinh 2\lambda\delta^+ - \sinh 2\lambda\delta^+}{\cosh 2\lambda\delta^+ + \cos 2\lambda\delta^+}\right)^2\right)} \tag{A3-2}$$

$$I_{\xi,r}(\sigma,\delta^+)$$
$$= \frac{1}{1+\lambda}\frac{(\cosh 2\lambda\delta^+ \cos 2\lambda\delta^+ - \sinh 2\lambda\delta^+ \sin 2\lambda\delta^+ + 1)(\cosh \lambda\sigma \cos \lambda\sigma + \sinh \lambda\sigma \sin \lambda\sigma)}{(\cosh 2\lambda\delta^+ + \cos 2\lambda\delta^+)^2} +$$
$$\frac{1}{1+\lambda}\frac{(\cosh 2\lambda\delta^+ \cos 2\lambda\delta^+ + \sinh 2\lambda\delta^+ \sin 2\lambda\delta^+ + 1)(\sinh \lambda\sigma \sin \lambda\sigma - \cosh \lambda\sigma \cos \lambda\sigma)}{(\cosh 2\lambda\delta^+ + \cos 2\lambda\delta^+)^2}$$

$$\tag{A3-3}$$

$$I_{f,w}(\sigma,\delta^+)$$
$$= \frac{\sinh 2\lambda\delta^+ - \sin 2\lambda\delta^+}{(1+\lambda)(\cosh 2\lambda\delta^+ + \cos 2\lambda\delta^+)}(\cosh \lambda\sigma \cos \lambda\sigma - \cosh \lambda\delta^+ \cos \lambda\delta^+)$$
$$+ \frac{\sinh 2\lambda\delta^+ + \sin 2\lambda\delta^+}{(1+\lambda)(\cosh 2\lambda\delta^+ + \cos 2\lambda\delta^+)}(\sinh \lambda\sigma \sin \lambda\sigma - \sinh \lambda\delta^+ \sin \lambda\delta^+) \tag{A3-4}$$
$$- \frac{1}{1+\lambda}(\sinh \lambda\sigma \cosh \lambda\sigma - \sinh \lambda\delta^+ \cosh \lambda\delta^+$$
$$+ \cosh \lambda\sigma \sin \lambda\sigma - \cosh \lambda\delta^+ \sin \lambda\delta^+) + (\sigma - \delta^+)$$